


Article

Transport Mechanism of Enhanced Performance in an Amorphous/Monoclinic Mixed-Phase Ga₂O₃ Solar-Blind Deep Ultraviolet Photodetector

Haowen Liu [†], Honglin Li [†], Shuren Zhou, Hong Zhang, Shiqiang Fan, Yuting Cui, Chunyang Kong, Lijuan Ye ^{*}, Yuanqiang Xiong ^{*} and Wanjun Li ^{* }

Chongqing Key Laboratory of Photo-Electric Functional Materials, College of Physics and Electronic Engineering, Chongqing Normal University, Chongqing 401331, China; liuhw2019@163.com (H.L.); 172093818@163.com (H.L.); srz19960715@163.com (S.Z.); zhh_2016@163.com (H.Z.); mikefan111@163.com (S.F.); cytcyt111@163.com (Y.C.); kchy@163.com (C.K.)

^{*} Correspondence: ylj2592924@163.com (L.Y.); xyq.0810@163.com (Y.X.); liwj@cqnu.edu.cn (W.L.); Tel.: +86-23-6536-2779 (L.Y.)

[†] H. Liu and H. Li contributed equally to this work.

Abstract: Recently, as an emerging material, ultrawide bandgap Ga₂O₃ has been investigated extensively in solar-blind deep-ultraviolet (DUV) photodetectors (PDs). High sensitivity and signal-to-noise ratio of PDs are essential for the detection of solar-blind DUV signals; however, such factors are often not mutually compatible. In the present study, an amorphous/monoclinic homogeneous mixed-phase structure was demonstrated to be significantly beneficial in enhancing the comprehensive performance of Ga₂O₃ solar-blind DUV PDs, especially with respect to sensitivity and the signal-to-noise ratio. Further experimental and theoretical findings provide insights on the transport mechanism of enhanced performance in the mixed-phase Ga₂O₃ solar-blind DUV PD. For effectively separating the photogenerated carriers, a type-II band alignment between amorphous and crystalline Ga₂O₃ can be exploited. Furthermore, the change of the barrier height of the mixed-phase interface also has a significant impact on the transport properties of the mixed-phase Ga₂O₃ PD. Additionally, the potential applications of mixed-phase Ga₂O₃ PD in high-voltage corona discharge were explored, and clear and stable corona discharge signals were obtained. The results of the present study may promote understanding of DUV photoelectronic devices with various mixed-phase Ga₂O₃ materials and provide an efficient approach for promoting comprehensive performance in future solar-blind detection applications.

Keywords: Ga₂O₃; mixed-phase structure; solar-blind photodetector; transport mechanism; DFT calculation



Citation: Liu, H.; Li, H.; Zhou, S.; Zhang, H.; Fan, S.; Cui, Y.; Kong, C.; Ye, L.; Xiong, Y.; Li, W. Transport Mechanism of Enhanced Performance in an Amorphous/Monoclinic Mixed-Phase Ga₂O₃ Solar-Blind Deep Ultraviolet Photodetector. *Crystals* **2021**, *11*, 1111. <https://doi.org/10.3390/cryst11091111>

Academic Editors: Haiding Sun, Bharat Jalan, Shibing Long, Yuhao Zhang, Rajendra Singh, Xuelin Yang, Yuji Zhao and Bin Liu

Received: 17 August 2021

Accepted: 8 September 2021

Published: 12 September 2021

Publisher's Note: MDPI stays neutral with regard to jurisdictional claims in published maps and institutional affiliations.



Copyright: © 2021 by the authors. Licensee MDPI, Basel, Switzerland. This article is an open access article distributed under the terms and conditions of the Creative Commons Attribution (CC BY) license (<https://creativecommons.org/licenses/by/4.0/>).

1. Introduction

Solar-blind deep-ultraviolet (DUV, 200~280 nm) photodetectors (PDs) with significant thermal stability and reliability have drawn considerable attention owing to the wide potential applications thereof in civil, military, and scientific research, such as high-voltage corona detection, flame detection, ozone holes monitoring, missile guidance, space communication, biochemical detection, and others [1–6]. At present, due to the relatively mature silicon technology, DUV detection is mainly dominated by silicon-based photodiodes [3], photomultiplier tubes (PMTs) [7], and charged-coupled devices (CCDs) [1,7]. However, mature silicon technology has several limitations in solar-blind DUV detection, which can be primarily attributed to the significant loss of the solar-blind region caused by the narrow bandgap of 1.13 eV [2]. In recent years, with the development of wide bandgap (WBG) semiconductor materials and devices, solar-blind DUV-PDs based on WBG materials have emerged, such as AlGa_N, MgZnO, ZnGaO, AlN, BN, diamond, and gallium oxide (Ga₂O₃) [4,8,9]. Among said materials, in addition to Ga₂O₃, other materials are more or

less subject to certain restrictions, such as high alloying causing reduced crystal quality and/or phase segregation [10], and larger bandgap leading to limited detection in the solar-blind region [11]. Owing to the suitable bandgap, good chemical stability, excellent thermal stability, high visible-light transparency, and other attributed thereof, the emerging ultrawide bandgap Ga₂O₃ material is a natural candidate material for next-generation solar-blind photodetectors [2,12].

Currently, Ga₂O₃ solar-blind DUV-PDs based on various material forms (bulk, thin films, and micro-/nanostructures) [13–16], different polymorphs (amorphous, α , β , γ , and ϵ -phase) [8,17–19] and diversified device structures (metal–semiconductor–metal (MSM) photodetectors, photodiodes, phototransistors, etc.) [20–24] have made significant progress. For the detection of solar-blind DUV signals, high sensitivity and signal-to-noise ratio of photodetectors are essential, which are mainly determined by high photocurrent and low dark current [1–3]. Since the intrinsic high-quality crystalline Ga₂O₃ has a larger resistivity, the PD generally obtains a lower dark current, often accompanied by a lower photocurrent [5,16,25]. Contrastingly, because the slow carrier detrapping process caused by internal defects usually produces a large internal gain, the defect-rich Ga₂O₃ (e.g., amorphous) solar-blind PD has high photocurrent and dark current [6,18,26]. As an example, Du et al. [18] observed that by increasing the oxygen flux during the sputtering process, the internal defects of the amorphous Ga₂O₃ films can be effectively suppressed, and the dark current of the PDs was significantly reduced, but the photocurrent was also reduced. By systematically comparing the optoelectronic properties of amorphous and crystalline Ga₂O₃ PDs, Qian et al. [25] found that the dark current and photocurrent of the amorphous Ga₂O₃ PD were higher than those of the crystalline PD. As such, finding a simple and effective method that can suppress dark current while increasing the photocurrent is the key to improving the performance of solar-blind DUV PDs. For instance, Mukhopadhyay et al. [27] reported that Sn doping could effectively suppress dark current and increase photocurrent of Ga₂O₃ solar-blind MSM PD through plasma-assisted molecular beam epitaxy.

Recently, mixed-phase semiconductor materials have been used in photodetectors, such as c-ZnMgO/w-ZnMgO, and others [10,28,29]. According to previous reports, PDs based on mixed-phase ZnMgO have been demonstrated to be able to achieve both higher responsivity (meaning higher photocurrent) and lower dark current, compared with single-phase structure devices [10,28,29]. For the Ga₂O₃ material, its different polymorphs are usually reported, namely α , β , γ , δ , ϵ , and even amorphous phase [1,30]. Among said polymorphs, α/β mixed-phase Ga₂O₃ including nanoarrays and thin film materials can be easily realized through the solution method and pulsed laser deposition method [17,31–33]. So far, based on α/β mixed-phase Ga₂O₃, research has been conducted in photocatalysis [31], water splitting [32], and solar-blind ultraviolet photodetectors [17]. In fact, Ga₂O₃ thin films prepared by sputter deposition at room temperature (RT) are usually amorphous [5,34]. By adjusting the growth or annealing temperature, the amorphous phase film can be crystallized and transformed into a monoclinic (β -phase) Ga₂O₃ film [34]. In such process, proper control of the growth or annealing temperature could achieve an amorphous/monoclinic mixed-phase Ga₂O₃ film (m-Ga₂O₃). Wu et al. [35] recently prepared an amorphous and crystalline mixed-phase Ga₂O₃ film and found that the performance of the mixed-phase Ga₂O₃ PD was enhanced. Despite such enhancement, the transport mechanism of mixed-phase Ga₂O₃ PD needs further improvement. Thus, there is a need for the preparation of amorphous/monoclinic m-Ga₂O₃ PD that have the aforementioned advantages of both individual amorphous and crystalline based PDs, and the further reveal of the transport mechanism of the mixed-phase Ga₂O₃ PD.

In the present study, as demonstrated by cross-sectional high-resolution transmission electron microscopy (HRTEM), a randomly distributed amorphous/monoclinic mixed-phase Ga₂O₃ thin film was obtained using radio frequency (rf) magnetron sputtering and postannealing treatment. The comprehensive performance of the MSM structure solar-blind DUV PD based mixed-phase Ga₂O₃ film was significantly enhanced, especially

in terms of sensitivity and signal-to-noise ratio. The detailed transport mechanism for the enhanced performance was experimentally and theoretically investigated, and the potential applications of mixed-phase Ga₂O₃ PD in high-voltage corona discharge were also explored. The present findings suggest that Ga₂O₃ composed of two mixed-phase structures is a competitive candidate for future application (such as detecting high-voltage corona) in high-performance solar-blind deep-ultraviolet photodetectors.

2. Experimental Details

Device Fabrication. A series of amorphous Ga₂O₃ films were prepared on (0001) sapphire (c-Al₂O₃) substrates by rf magnetron sputtering at RT, and the detailed procedures are provided in the supplementary (Note 1). To realize the amorphous/monoclinic mixed-phase Ga₂O₃ film (m-Ga₂O₃), part of the samples underwent isochronal annealing at 100, 200, 300, 400, and 500 °C in an argon atmosphere, labeled as S100, S200, S300, S400, and S500, respectively. The reference sample without postannealing was named SRT. Based on said samples, MSM solar-blind DUV-PDs were fabricated. The contact electrodes were deposited by a conventional mask process. The made-up device comprised three pairs of interdigital electrodes (Ti/Au (30/100 nm)) that were 200 μm, 200 μm, and 2800 μm in spacing, width, and length, respectively.

Characterization. The crystallinity analysis of the material was conducted using X-ray diffraction (XRD, Bruker D8 ADVANCE A25X), and monochromatic Cu Kα1 radiation ($\lambda = 1.540598 \text{ \AA}$) was used as the X-ray source. Raman spectra were obtained using a Horiba HR Evolution Raman spectrometer equipped with a $\times 50$ lens, and the excitation wavelength was 532 nm. The TEM lamella of a mixed-phase Ga₂O₃ film deposited on c-plane sapphire was prepared through focused ion beam (FIB) milling using a FEI HELIOS NanoLab 600i. A Titan G2 60-300 Transmission Electron Microscope operating at 300 keV was used to obtain cross-sectional high-angle annular dark-field (HAADF) HRTEM images and EDX mappings. The transmittance and absorption spectra of Ga₂O₃ films were measured with a UV–vis–near infrared spectrophotometer (Hitachi U4100). The chemical composition and valence state were analyzed using X-ray photoelectron spectroscopy (XPS) (ESCALAB 250Xi, Thermo Scientific (Massachusetts, USA)). The current–voltage (I–V) characteristics and time-dependent photoresponse of the Ga₂O₃ MSM PDs were investigated using Keithley 2450. To provide light of 254 and 365 nm wavelengths for the photoresponse measurement, a low-pressure lamp was used as the UV illumination source.

3. Results and Discussion

Figure 1a shows the XRD patterns of Ga₂O₃ films upon increasing the annealing temperature from RT to 500 °C. In the samples annealed between RT to 400 °C (SRT to S400), no signature peak was observed. However, regarding the sample annealed at 500 °C (S500), three distinct peaks were located near 18.40°, 37.90°, and 58.71°, corresponding to the (201), (402), and (603) planes of monoclinic Ga₂O₃ (β -Ga₂O₃) (PDF#43-1012) [15]. Figure 1b presents the Raman scattering spectra of Ga₂O₃ films annealed at different temperatures. Similar to the XRD results, aside from the substrate-related vibration modes, no vibration mode was observed in SRT-S300. Meanwhile, in S500, a vibration mode located at $\sim 201 \text{ cm}^{-1}$ was observed, which originated from the vibration and translation of tetrahedron/vibration chain of β -Ga₂O₃ [36]. Hence, postannealing can promote the phase transition from amorphous to monoclinic Ga₂O₃, which is consistent with the results of previous reports [34]. Notably, a considerably weak vibration mode located at $\sim 201 \text{ cm}^{-1}$ was also observed in S400, indicating that S400 may have nanocrystals, that is, S400 may be a mixed-phase film constructed of amorphous and monoclinic Ga₂O₃.

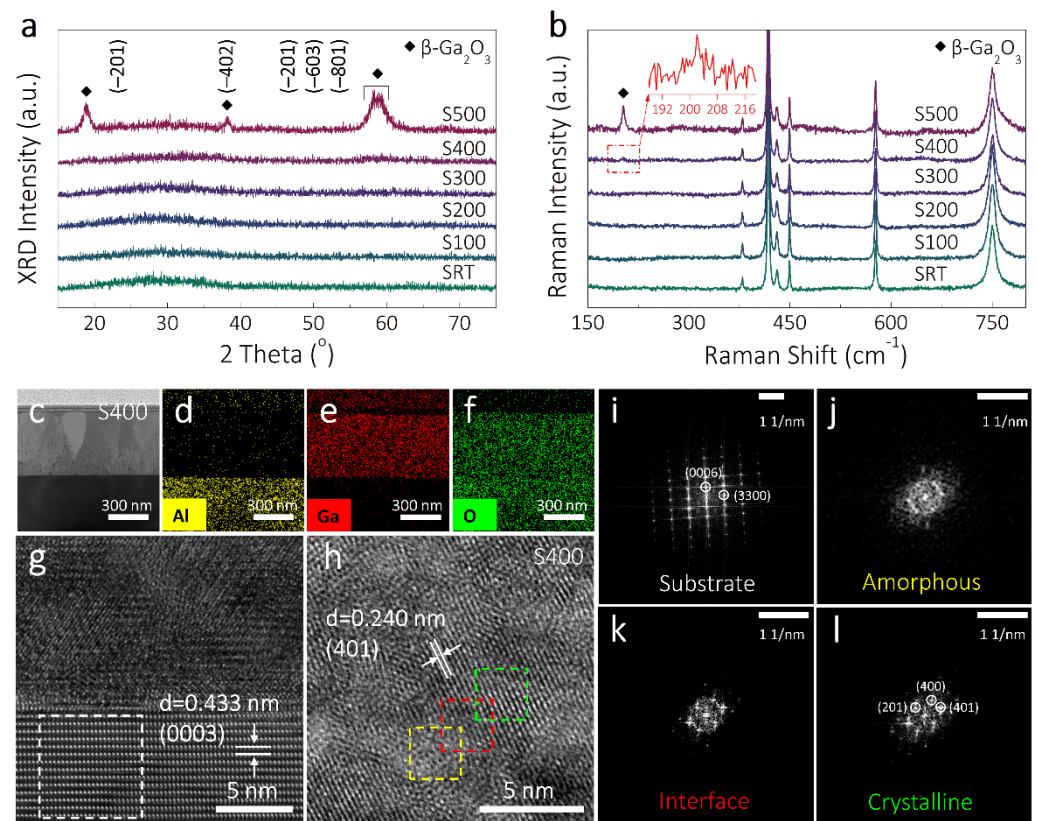


Figure 1. XRD pattern (a) and Raman scattering spectra (b) of Ga₂O₃ films annealed with different temperatures. (c) The SEM image of the cross-section of mixed-phase Ga₂O₃ (S400) and the corresponding EDX elemental mapping images of Al (d), Ga (e), and O (f). (g) Cross-sectional TEM image of Ga₂O₃/c-Al₂O₃ interface (S400). (h) Magnified HRTEM image of mixed-phase Ga₂O₃ film, the yellow, red, and green dotted selected areas correspond to the amorphous, interface, and crystalline regions, respectively. FFT pattern of substrate (i), amorphous region (j), amorphous/crystalline interface (k), and crystalline region (l).

To verify whether sample S400 was a mixed-phase film, cross-sectional high-resolution transmission electron microscopy (HRTEM) sample was prepared with a FEI Helios dual beam focused ion beam (FIB). Figure 1c shows the SEM image of the cross-section and the corresponding energy dispersive X-ray (EDX) elemental mapping images of Al (Figure 1d), Ga (Figure 1e), and O (Figure 1f), revealing that a film thickness of about ~490 nm, and Ga and O elements were uniformly distributed in the whole film with a clear interface structure. Further supporting evidence can be seen in the HRTEM image of the substrate with a zone axis of Al₂O₃ (1100) shown in Figure 1g [37], a lattice parameter of 0.432 nm corresponds to the (0003) plane of the c-plane sapphire substrate, and there is a clear abrupt interface between the film and sapphire substrate, and no obvious buffer or nucleation layer is observed. Figure 1i presents the fast Fourier transform (FFT) image corresponding to the white dotted selected area in Figure 1g, in which two sets of diffraction spots coming from the (0006) and (3300) plane of the substrate can be observed, indicating the highly ordered lattice array of the c-plane Al₂O₃ substrate. To investigate the amorphous and crystalline regions in the Ga₂O₃ films, high-angle annular dark-field (HAADF) HRTEM images of the sample S400 were taken. The amorphous/crystalline regions in the HRTEM image acquired from the S400 can be identified from the contrast (see Figure 1g,h). The yellow, red, and green dotted selected areas correspond to the amorphous, interface, and crystalline regions, respectively. In Figure 1h, the lattice parameter of the crystalline region was measured to be 0.24 nm, corresponding to the (401) plane of β -Ga₂O₃ [31]. Figure 1j–l represent the FFT images in Figure 1h. An observation can be made that the transition occurred from

the diffraction ring (amorphous region) to the clear lattice (crystalline region), with the diffraction spots corresponding to the (201), (401), and (400) plane of β - Ga_2O_3 . Figure S1 shows the HRTEM images of different regions of the S400. Obviously, there were randomly distributed crystalline phases Ga_2O_3 in different regions, indicating that the amorphous and crystalline phases were continuously distributed in sample S400. Therefore, sample S400 was clearly demonstrated to be a mixed-phase film, which consisted of amorphous domains and crystalline grains with random orientations.

To compare the solar-blind photoelectric characteristics of the mixed-phase Ga_2O_3 film (m- Ga_2O_3) and the others, the metal–semiconductor–metal (MSM) structured DUV PDs with Ti/Au interdigital electrodes (see inset of Figure 2a) were fabricated for photoresponse measurement, and the detailed procedure is provided in the Experimental Section. The I–V characteristics curves of Ga_2O_3 film PDs (SRT-S500) under dark, 365 nm, and 254 nm illumination (the light intensity of 254 nm is 100–700 $\mu\text{W}/\text{cm}^2$, and the light intensity of 365 nm is 500 $\mu\text{W}/\text{cm}^2$) are shown in Figure S2a–f. An observation can be made that the six devices could be considered as back-to-back Schottky barriers due to the apparently nonlinear I–V characteristics [38], and the photocurrent generated by PDs could be primarily determined by the number of photogenerated carriers under DUV light illumination [39]. As the light intensity increased from 100 to 700 $\mu\text{W}/\text{cm}^2$, the photocurrent increased almost linearly, as shown in Figure S2g. Notably, m- Ga_2O_3 PD (S400) had the largest photocurrent under all ultraviolet light intensities, and the slope of the I–V characteristics curve of such device was also the largest, indicating that mixed-phase Ga_2O_3 PD had the strongest light dependence and internal gain. Figure S3 shows the dark current and photocurrent variation curves of Ga_2O_3 PDs, and an observation can be made that as the Ga_2O_3 film gradually crystallized, the dark current of the PD decreased continuously, and the decrease of the mixed-phase Ga_2O_3 PD was more significant. The aforementioned conclusions indicate that the mixed-phase Ga_2O_3 PD not only had a larger gain but also had a lower dark current. Figure 2a also shows the photocurrent variation of S400 with light intensity, and more detailed current changes under logarithmic coordinate at 254 nm, 365 nm, and dark conditions are shown in Figure 2b. As demonstrated in Supplementary Information (Note 2), main performance indexes such as responsivity (R), detectivity (D^*), external quantum efficiency (EQE), photo-to-dark current ratio (PDCR), and rejection ratio (R_{254}/R_{365}) were calculated using corresponding equations, so as to further quantitatively compare the optoelectronic properties of the mixed-phase Ga_2O_3 PD and the other five devices. The calculation results of R, D^* , EQE, PDCR, and R_{254}/R_{365} of all six PDs under 5 V bias voltage and 500 $\mu\text{W}/\text{cm}^2$ are shown in Figure 2d–h. As shown, the comprehensive performance of mixed-phase Ga_2O_3 PD was significantly superior compared with the other devices, with high responsivity (1.31 A/W), detectivity (1.35×10^{13} Jones), and external quantum efficiency (640.5%), in addition to significant photo-to-dark current ratio (2.20×10^4) and rejection ratio (1.20×10^5). The results demonstrated that the mixed-phase Ga_2O_3 can simultaneously improve the sensitivity and signal-to-noise ratio of the PD, which is more conducive to the application of the device in solar-blind DUV signal detection [2].

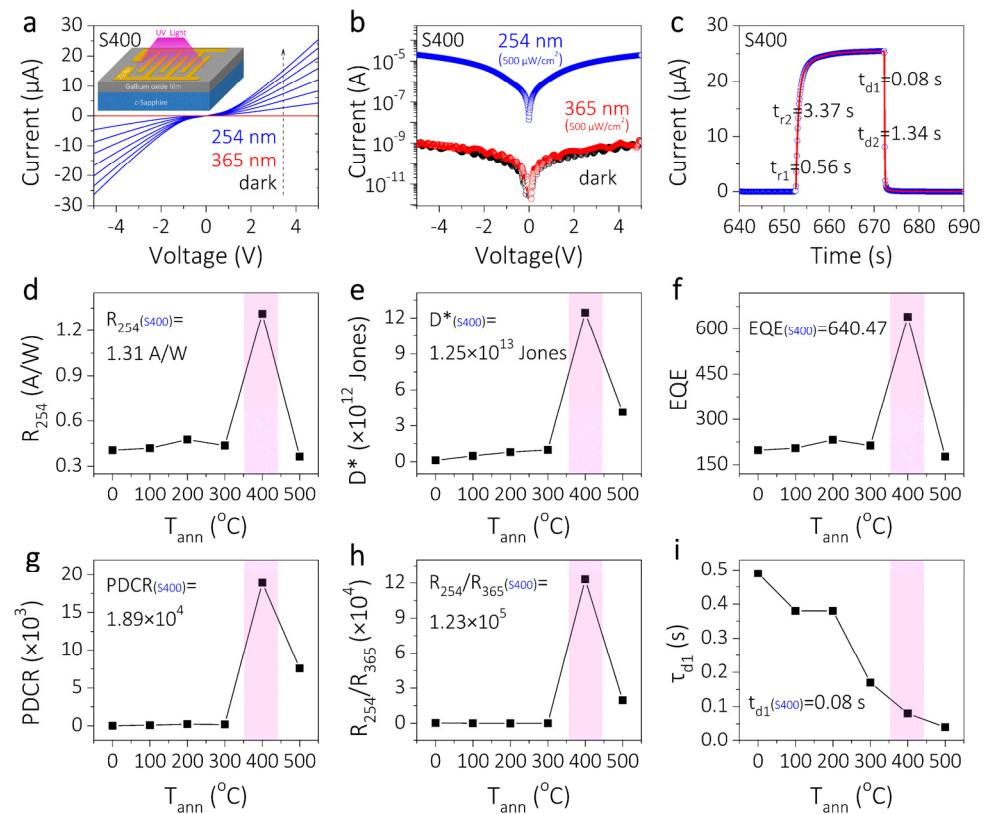


Figure 2. (a) I–V characteristics of mixed-phase Ga₂O₃ PD (S400) under dark, 365 nm, and 254 nm illumination (the light intensity of 254 nm is 100–700 $\mu\text{W}/\text{cm}^2$, and the light intensity of 365 nm is 500 $\mu\text{W}/\text{cm}^2$), and the inset shows the structure diagram of MSM structured Ga₂O₃ PD. (b) I–V characteristics of S400 under dark and illumination with 254 nm/365 nm UV light (500 $\mu\text{W}/\text{cm}^2$) on a logarithmic scale. (c) Enlarged view of the single response (blue) of S400 and the corresponding fitted rise and decay times (red). (d–i) Plots of R, D*, EQE, PDCR, R_{254}/R_{365} , and τ_{d1} versus postannealing temperature.

Figure S4 presents the time dependence of photoelectric properties of all six PDs with the switching of 254 nm light (500 mW/cm^2) under the bias of 5 V. The photocurrent responded immediately as the light was turned on, revealing the instantaneous accumulation of photogenerated carriers [40]. Subsequently, the radiation transition and recombination tended to balance, thereby presenting a stationary photocurrent [39]. All PDs could be reversibly modulated by 254 nm illumination, and the photocurrent exhibited significant reproducibility even under continuous operation for 70 cycles. For a more detailed comparison of the photoresponses, the quantitative investigations were expressed by the fitting of the time-dependent photocurrent curves with a biexponential relaxation equation [41] (see Supplementary Information (Note 2)). The rise (τ_r) and decay times (τ_d) of all PDs were well fitted as shown in Figure S4. An observation can be made that the τ_r of all devices remained basically stable during the crystallization process of Ga₂O₃ films, but the τ_d gradually accelerated, particularly in S400 and S500. As shown in Figure 2c, the fast components of τ_r and τ_d of m-Ga₂O₃ PD (S400) were counted to be $\tau_{r1} = 0.56$ s and $\tau_{d1} = 0.08$ s, respectively. Among said components, the fast decay component (τ_{d1}) of S400 was significantly faster than the other amorphous devices (SRT-S300) and was considerably close to the value of the crystalline device (S500) (see Figure 2f). The comprehensive performance of the present mixed-phase Ga₂O₃ PD was significantly enhanced with not only high sensitivity and signal-to-noise ratio but also fast response, and the device also exhibited a more balanced performance in the reported results, as shown in Table 1.

Table 1. Detailed comparison between previously reported Ga₂O₃ PDs with the present mixed-phase Ga₂O₃ solar-blind DUV PD.

Materials	Structures	Responsivity (A/W)	Detectivity (Jones)	EQE (%)	PDCR	Rejection Ratio	Decay Time (s)	Ref.
a-GaO _x /β-Ga ₂ O ₃	MSM	1.31	1.34 × 10 ¹³	6.4 × 10 ²	2.21 × 10 ⁴	1.2 × 10 ⁵	0.08	This work
Ga ₂ O ₃	MSM	3.30	4.00 × 10 ¹²	1.6 × 10 ³	10	2.0 × 10 ³	0.02	[13]
Ga ₂ O ₃	MSM	26	1.25 × 10 ¹³	1.4 × 10 ⁴	10 ⁴	3.0 × 10 ²	0.18	[14]
Ga ₂ O ₃	MSM	29.80	1.00 × 10 ¹²	-	10 ³	9.4 × 10 ³	-	[42]
a-/c-Ga ₂ O ₃	MSM	0.81	5.67 × 10 ¹⁴	4.0 × 10 ²	1.2 × 10 ⁷	8.1 × 10 ⁵	2 × 10 ⁻⁵	[30]
Diamond/Ga ₂ O ₃	MSM	0.20	6.90 × 10 ⁹	-	242	1.2 × 10 ²	-	[11]
Ga ₂ O ₃ : Mn	MSM	0.07	-	3.6 × 10 ¹	67	-	0.03	[43]
MoS ₂ /Ga ₂ O ₃	Heterojunction	2.05	1.21 × 10 ¹¹	-	670	1.6 × 10 ³	-	[44]
ZnO/Ga ₂ O ₃	Heterojunction	9.70	6.29 × 10 ¹²	-	>10 ⁴	6.9 × 10 ²	0.09	[45]
ZnO: Ga/Ga ₂ O ₃	Heterojunction	3.73	-	-	>10 ²	10 ²	0.272	[46]
SnO ₂ /CuZnS	Heterojunction	0.0016	5.41 × 10 ¹¹	-	1.3 × 10 ³	-	0.001	[47]
GaN/Ga ₂ O ₃ : Sn	<i>p-n</i>	3.05	1.69 × 10 ¹³	-	~10 ⁴	5.9 × 10 ³	0.018	[48]
CuSCN/Ga ₂ O ₃	<i>p-n</i>	0.0013	9.43 × 10 ¹¹	-	4.14 × 10 ⁴	1.2 × 10 ⁴	0.035	[49]
Graphene/Ga ₂ O ₃	Schottky	39.30	5.92 × 10 ¹³	2.0 × 10 ⁴	3.40 × 10 ²	-	219	[20]
<i>p-Gr</i> /AlN	Schottky	0.067	-	4.3 × 10 ¹	10 ³	10 ³	4 × 10 ⁻⁴	[50]

To unravel the transport mechanism of enhanced performance in an amorphous/monoclinic mixed-phase Ga₂O₃ solar-blind photodetector, further research was conducted in combination with experimental and theoretical calculations. The interface between insulating oxide channels is considerably important, and the band offset at the edges of the conduction band and valence band largely determines the PD performance [51,52]. According to the method proposed by Kraut et al. [53], by extracting scanning data from the X-ray photoelectron spectroscopy (XPS), the band alignment of amorphous/monoclinic mixed-phase Ga₂O₃ can be obtained. Figure S5a shows a schematic diagram of the XPS test. An amorphous sample was first fully annealed at 900 °C to obtain a completely crystalline layer (crystalline Ga₂O₃), and then half-covered with a completely amorphous layer (amorphous Ga₂O₃). Figure 3a,b show the energy level of crystalline and amorphous Ga₂O₃. The valence band maximum (VBM)/Ga 2p_{3/2} values of crystalline and amorphous Ga₂O₃ were 2.06/1117.30 eV and 2.57/1117.60 eV, respectively. Additionally, to measure the absorption spectra of amorphous and crystalline samples, an ultraviolet–visible–infrared spectrophotometer was used (see Figure S5b for the schematic diagram), and the bandgaps of the amorphous and crystalline Ga₂O₃ films were calculated to be 4.64 eV and 4.92 eV, respectively. According to said values, the band offsets in valence band ΔE_V and conduction band ΔE_C were found to be 0.51 eV and 0.80 eV, respectively, and a more detailed description of amorphous/crystalline Ga₂O₃ band alignment calculation is described in Supplementary Information (Note 3). The band alignment schematic of the amorphous/crystalline interface are provided in Figure 3c, indicating that a typical staggered type-II band alignment was obtained, thereby potentially promoting the carriers transport by electric potential [51,54]. As shown in Figure 3d [51,52,54–64], the present mixed-phase Ga₂O₃ films had a large band offset including ΔE_V and ΔE_C compared with previous research. The band offset of m-Ga₂O₃ film in the present study completely meets the interface’s requirements for the driving force of separating electron–hole pairs.

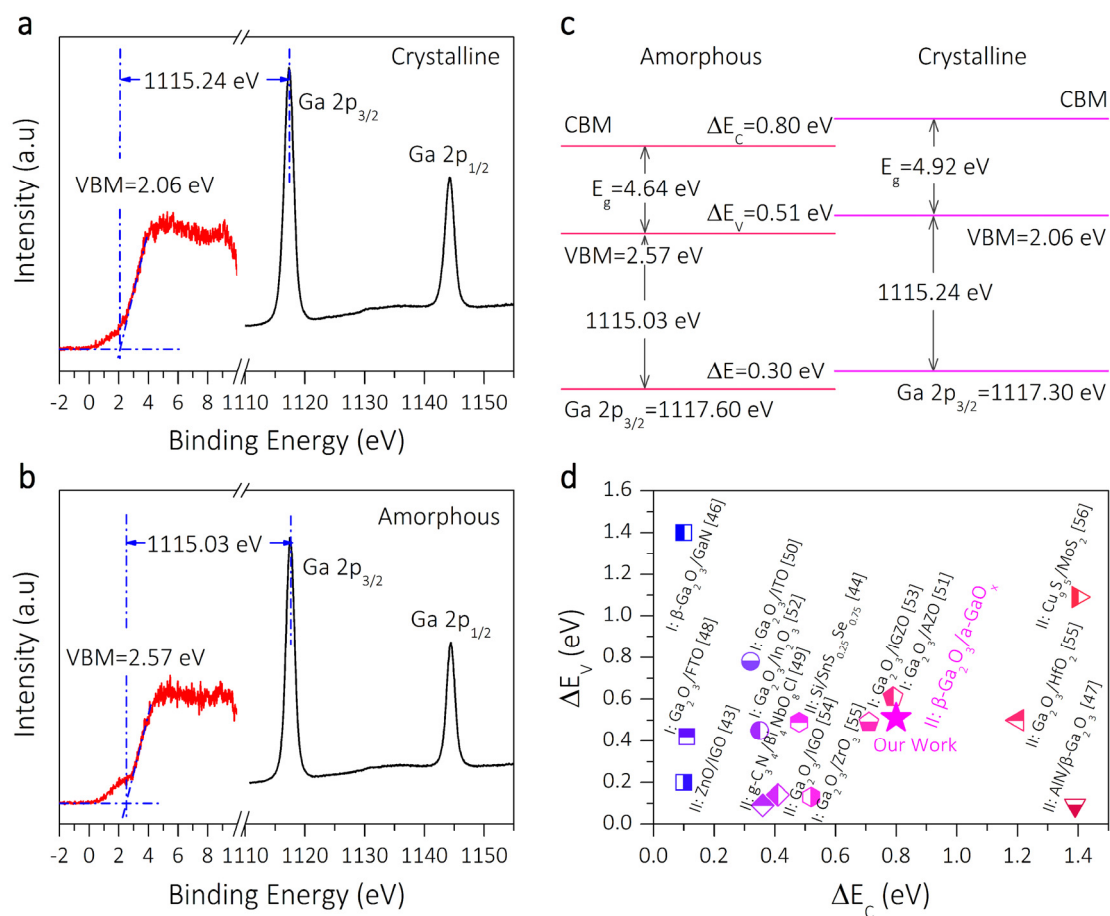


Figure 3. XPS valence band spectra and Ga 2p core level of crystalline (a) and amorphous (b) Ga₂O₃ films. (c) Schematic illustration of energy band alignment of amorphous/crystalline Ga₂O₃. (d) Comparison between previously reported conduction and valence band offsets of heterojunction with our amorphous/crystalline Ga₂O₃ [51,52,54–64].

DFT calculations were further performed to explore electronic characteristics of amorphous/crystalline mixed-phase Ga₂O₃. Based on the aforementioned TEM results, the (401) plane d-spacing was dominated. As such, an interface was constructed with crystalline β-Ga₂O₃ and amorphous Ga₂O₃ along (401), as shown in Figure 4a. During the relaxation process, several layers of Ga₂O₃ atoms near the interface were allowed to interact. To optimize the structure with cutoff energy of 500 eV, the Perdew–Berk–Ernzerhof (PBE) exchange correlation function was used. For the mixed-phase model, the Monkhorst–Pack *k*-point grid was set to 1 × 11 × 2, and the force threshold was set to 0.01 eV/Å. The energy convergence tolerance was 10^{−4} eV [65].

The difference in charge density perpendicular to the interface was explored, so as to understand the charge transfer and charge distribution between crystalline and amorphous phase Ga₂O₃ after the interface was formed. The difference in charge density is defined as [66]:

$$\Delta\rho(z) = \rho_{\text{mixed}} - \rho_{\text{crystalline}} - \rho_{\text{amorphous}} \quad (1)$$

where ρ_{mixed} , $\rho_{\text{crystalline}}$, and $\rho_{\text{amorphous}}$ are the charge density of mixed, crystalline, and amorphous phase Ga₂O₃, respectively. As shown in Figure 4b, the cyan and yellow regions represent the depletion and accumulation of charges in the space, respectively. Obviously, the charge transfers mainly occurred between the contact parts, which could lead to an effective separation of light generated carriers in this polarization field. The difference in charge indicates the charge transfer direction from the crystalline Ga₂O₃ to the amorphous Ga₂O₃ [67].

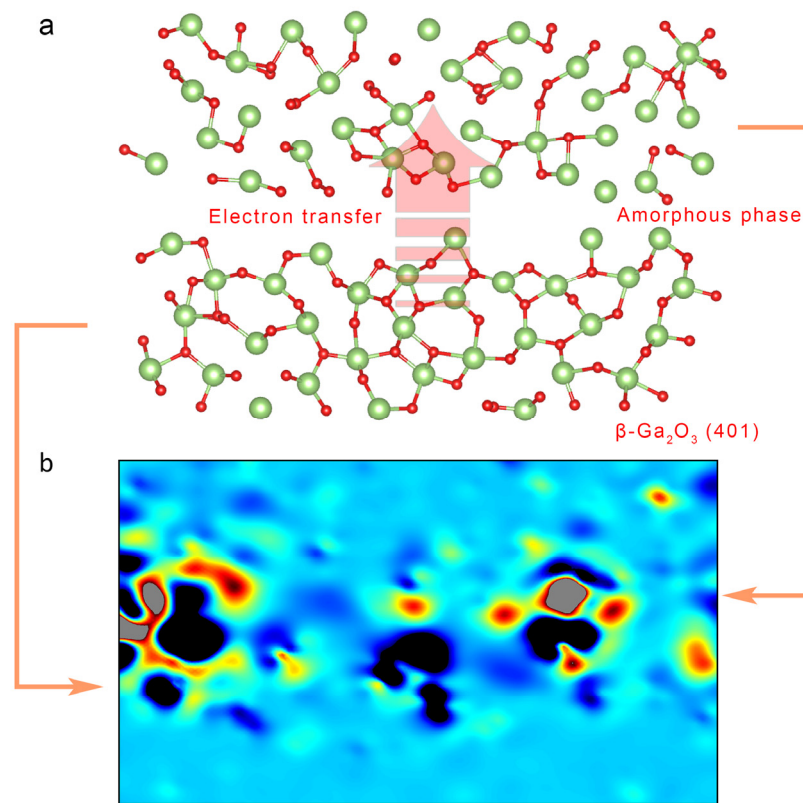


Figure 4. (a) Mixed phase of β -Ga₂O₃ and amorphous structure. The pink arrow denotes the direction of charge transfer and the built-in electric field. (b) Charge density difference in the mixed phase. The red and blue areas signify the accumulation and depletion of electrons, respectively.

Figure 4a also shows a schematic diagram of light-induced carrier transfer in the mixed phase. The formation of said mixed phase will cause the redistribution of charges. The results show that the electrostatic intervention can make the amorphous phase negatively charged, while the crystal phase is positively charged. When two parts finally reach the same Fermi level, the built-in electric field from the crystalline phase to the amorphous phase will prevent the charge from diffusing [68,69]. Such a built-in electric field will act as a driving force to separate photogenerated carriers into different layers and can effectively prevent the recombination of photogenerated carriers. Through the separation of said carriers, the life of e^-h^+ can be effectively prolonged, and the overall performance will be promoted. Such theoretical calculation results agree with the aforementioned experimental analysis.

Based on the aforementioned results, the following mechanism is proposed to explain the enhanced performance of the mixed-phase Ga₂O₃ solar-blind photodetector, which is schematically introduced in Figure 5. The previous results show that the crystalline and amorphous domains in the mixed-phase Ga₂O₃ film (S400) are randomly distributed, and the mixed-phase structure presents a typical staggered type-II band alignment (see Figure 5a). To maintain the equilibrium of the mixed-phase interface Fermi level, the electrons in the crystalline Ga₂O₃ will migrate to the amorphous Ga₂O₃, thereby inducing the energy levels near the amorphous Ga₂O₃ bending upwards to form a built-in electric field (space charge region) around the interface. When two parts finally reach the same E_f , the built-in electric field from the crystalline phase to the amorphous one will prevent the further diffusion of charges [10,28].

The dark current transport process of mixed-phase Ga₂O₃ PD under a bias of 5 V is shown in Figure 5b. In general, a large number of oxygen vacancies acting as donor states in the amorphous Ga₂O₃ is beneficial for prolonging the life of electrons and inducing photoconductivity gain [10]. At the same time, a high density of oxygen vacancies has

a high intrinsic carrier concentration [25], leading to lower resistivity and a large dark current of amorphous Ga_2O_3 . However, the mixed-phase Ga_2O_3 PD exhibited a low dark current and can be explained as follows. Ga_2O_3 is a natural n -type oxide semiconductor material [2,3,70]. According to the traditional theory of n - n heterojunction, the bias voltage applied to wide bandgap semiconductor is predominantly concentrated at the interface between different phase parts [28]. Since the crystalline and amorphous domains of mixed-phase Ga_2O_3 are considerably small, V_1 and V_2 are, respectively, approximated as the voltage applied to the interface between crystalline and amorphous domains. For defects such as oxygen vacancies, the resistivity of amorphous domains is smaller than that of crystalline domains, such that the voltage V_1 added on crystalline domains is higher than the voltage V_2 added on amorphous domains. Thus, the heights of the two barriers for electrons and one barrier for holes are $q(V_{D1} + V_1)$, $q(V_{D2} - V_2)$ and $\Delta E_C - q(V_{D2} - V_2)$, respectively. Thereinto, qV_{D1} and qV_{D2} are the barrier heights of electrons and holes without bias voltage, and ΔE_C is the conduction band offset. The transfer of most electrons is blocked due to the presence of a high-density barrier layer at the interface between Ga_2O_3 domains of different phases, which is primarily responsible for the low dark current of the present mixed-phase Ga_2O_3 PD.

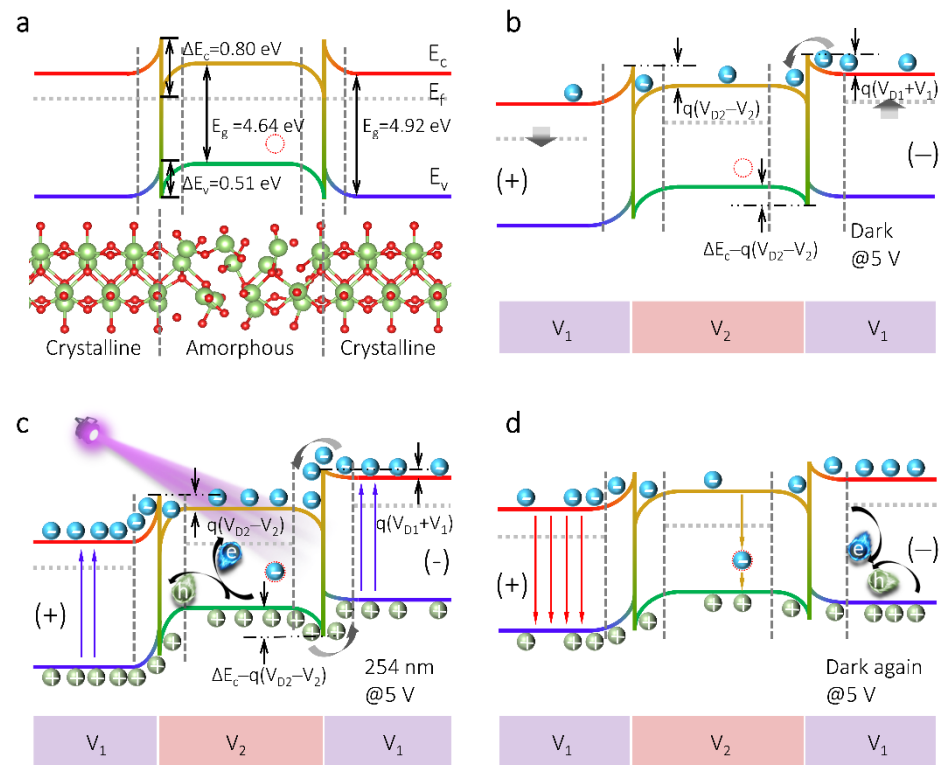


Figure 5. Energy band diagram and carrier transport process of amorphous/crystalline mixed-phase Ga_2O_3 PD at different conditions: (a) after contact without bias, (b) under bias in dark, (c) under bias with 254 nm DUV illumination, and (d) in dark again after photoexcitation.

Figure 5c displays a schematic illustration of solar-blind ultraviolet light on the amorphous/crystal interface. The high-energy light will stimulate the $m\text{-Ga}_2\text{O}_3$ film to rapidly excite many electrons into the conduction band and leave holes in the valence band of both amorphous and crystalline Ga_2O_3 . Hence, the resistance of both Ga_2O_3 domains will decrease. However, because of the higher defect concentration of amorphous domains, the resistivity thereof is lower than that of the crystalline. Compared with the amorphous Ga_2O_3 , the photogenerated carriers caused the resistivity of the crystalline domains to decrease more [71], such that V_2 increased to be larger than V_1 . After that, the two barriers of electrons at the interface were lowered, which promoted the transport of photogenerated

electrons. On the contrary, the barriers of holes were raised, meaning that the photocurrent was mainly composed of electrons [72]. As such, the mixed-phase based PD exhibited a photocurrent much higher than the dark current. Furthermore, according to the previous results, the photocurrent of mixed-phase based PD was significantly greater than that of other five devices, which is usually related to the effective separation and prolonged lifetime of carriers [22]. The present experimental and theoretical results all reveal that the charge transfer mainly occurred in the mixed phase interface, potentially leading to the effective separation of light-induced carriers under such polarization field. Moreover, the ΔE_V and ΔE_C at the amorphous/crystal interface were 0.5 and 0.8 eV, respectively, and the mixed phase interface presented a type II band alignment. Such band offset will act as a driving force to separate photogenerated carriers into different layers, which is a key mechanism that can restrain recombination processes and extend the life of light-induced carriers, resulting in a significant enhancement in photocurrent. In fact, an assumption can be made that such mechanism will exist in all devices with crystalline/amorphous interfaces. However, as the thin film gradually crystallized, the number of crystalline/amorphous interfaces first increased and then decreased, and the presence of continuous amorphous (S100–S300) or crystalline (S500) may also affect such mechanism. Ultimately, the best crystalline/amorphous interface arrangement was obtained in S400, which may be the reason for S400 having the best performance. In addition, since many oxygen vacancies in amorphous Ga_2O_3 act as electron traps [18,25], when UV illumination was turned on, the photogenerated electrons were captured by the oxygen vacancies. Hence, the life of electrons can be effectively prolonged, promoting enhancement of the photocurrent. Finally, the mixed-phase Ga_2O_3 PD had the highest photocurrent and enhanced performance by effectively separating photogenerated carriers and prolonging the lifetime thereof.

Figure 5d shows that when the ultraviolet light was turned off, the photogenerated electron–hole pairs recombined rapidly. In general, the amorphous domain could trap electrons and induce gain, in addition to slowing down the recombination of electrons in the device. However, the present mixed-phase solar-blind PD still achieved rapid decay time due to the rapidly established barrier at the mixed-phase interface.

Corona discharge detection is an important application for solar-blind ultraviolet photodetectors [4]. Owing to the existence of weak solar-blind signals in the exposed high-voltage cables and components, the Ga_2O_3 based photodetector can be placed further away from the arc for long-distance and wide-angle detection if stable and highly sensitive detection can be achieved. In order to explore the corona discharge detection capability of m- Ga_2O_3 PD, a simple corona discharge test system was constructed, as shown in Figure 6. Figure 6a shows the photograph of the intensity test of the ~254 nm deep ultraviolet light generated by the corona simulator (lighter). The radiometer shows that the intensity was only $0.4 \mu\text{W}/\text{cm}^2$. As shown in Figure 6b, the corona detection environment was simulated under sunlight, and the photoresponse of m- Ga_2O_3 PD is shown in Figure 6c. When the lighter was discharged, the device responded repeatedly with a photocurrent signal of about 30–50 nA. Such result indicates that the solar-blind ultraviolet photodetector based on m- Ga_2O_3 film had significant sensitivity and has potential applications in high-voltage corona discharge and other fields.

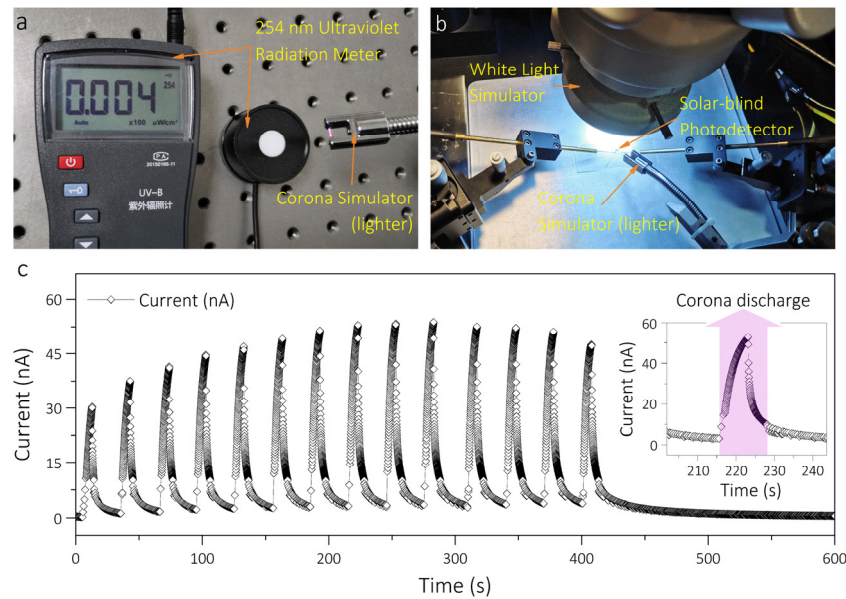


Figure 6. (a) Irradiation intensity test of corona simulator discharge; (b) a photograph of $m\text{-Ga}_2\text{O}_3$ solar-blind PD performing a corona discharge simulation test on a probe station; (c) time-dependent corona discharge photoresponse of $m\text{-Ga}_2\text{O}_3$ solar-blind PD, the inset shows the photoresponse of a single corona discharge, and the purple area is the corona discharge process.

4. Conclusions

In summary, simultaneously enhanced sensitivity and signal-to-noise ratio of MSM solar-blind DUV PD based on an amorphous/monoclinic homogeneous mixed-phase structure Ga_2O_3 film was reported, and the transport mechanism was discussed in detail. The present mixed-phase Ga_2O_3 solar-blind DUV PD exhibited a high R of 1.31 A/W , D^* of $1.35 \times 10^{13} \text{ Jones}$, and EQE of 640.5%, in addition to significant PDCR of 2.20×10^4 and rejection ratio ($R_{254 \text{ nm}}/R_{365 \text{ nm}}$) of 1.20×10^5 , thereby demonstrating high sensitivity and signal-to-noise ratio of the PD. Additionally, a fast recovery speed of 80 ms was achieved, which is significantly faster than other amorphous devices, and is considerably close to the value of the crystalline device. In combination with experimental and theoretical investigations, the results of the present study demonstrate that the band offset and barrier height difference of the mixed-phase interface were responsible for enhancing the comprehensive performance of Ga_2O_3 solar-blind DUV PDs. Moreover, based on the mixed-phase Ga_2O_3 PD, the potential application in the detection of high-voltage corona discharge was explored, and a clear and stable corona discharge detection signal was obtained. The present findings may contribute to a better understanding of the enhanced performance in the mixed-phase DUV photoelectronic devices and provide an efficient approach for promoting comprehensive performance in future solar-blind detection applications.

Supplementary Materials: The following are available online at <https://www.mdpi.com/article/10.3390/cryst11091111/s1>. See the supplementary material for detailed information on the HRTEM images of the mixed-phase Ga_2O_3 (Figure S1), the I–V characteristics curve (Figure S2), dark current and photocurrent variation curves (Figure S3) and transient response (Figure S4) of Ga_2O_3 PDs, determination of bandgap of Ga_2O_3 films (Figure S5), the deposition of the Ga_2O_3 thin films (Note 1), the main performance index calculations of PDs (Note 2), and the band alignment calculation of the mixed-phase Ga_2O_3 (Note 3).

Author Contributions: Conceptualization, W.L.; methodology, H.L. (Haowen Liu), S.Z., Y.X.; software, H.L. (Honglin Li); formal analysis, W.L., H.L. (Haowen Liu), H.L. (Honglin Li), S.Z.; investigation, H.L. (Haowen Liu), H.L. (Honglin Li), W.L., S.Z., H.Z., L.Y., Y.X.; resources, S.F., Y.C., C.K.; data curation, H.L. (Haowen Liu), H.L. (Honglin Li), Y.X.; writing—original draft preparation, H.L. (Haowen Liu), H.L. (Honglin Li); writing—review and editing, W.L., L.Y., Y.X.; supervision, W.L., Y.C., C.K., L.Y.; project administration, W.L.; funding acquisition, W.L., H.Z., L.Y. All authors have read and agreed to the published version of the manuscript.

Funding: This research received no external funding.

Institutional Review Board Statement: Not applicable.

Informed Consent Statement: Not applicable.

Data Availability Statement: The data that support the findings of this study are available from the corresponding author upon reasonable request.

Acknowledgments: The authors gratefully acknowledge support from the National Natural Science Foundation of China (Grant Nos. 11904041 and 51472038), the Natural Science Foundation of Chongqing (Grant Nos. cstc2020jcyj-msxmX0557, cstc2020jcyj-msxmX0533 and cstc2019jcyj-msxmX0237) and the Science and Technology Research Project of Chongqing Education Committee (Grant Nos. KJQN201900542, KJQN202000511 and KJQN201800501).

Conflicts of Interest: The authors declare no conflict of interest.

References

1. Pearton, S.J.; Yang, J.; Cary, P.H.; Ren, F.; Kim, J.; Tadjer, M.J.; Mastro, M.A. A review of Ga₂O₃ materials, processing, and devices. *Appl. Phys. Rev.* **2018**, *5*, 011301. [[CrossRef](#)]
2. Xu, J.; Zheng, W.; Huang, F. Gallium Oxide Solar-Blind Ultraviolet Photodetector: A Review. *J. Mater. Chem. C* **2019**, *7*, 8753–8770. [[CrossRef](#)]
3. Xie, C.; Lu, X.; Tong, X.; Zhang, Z.; Liang, F.; Liang, L.; Luo, L.; Wu, Y. Recent Progress in Solar-Blind Deep-Ultraviolet Photodetectors Based on Inorganic Ultrawide Bandgap Semiconductors. *Adv. Funct. Mater.* **2019**, *29*, 1806006. [[CrossRef](#)]
4. Chen, X.; Ren, F.; Gu, S.; Ye, J. Review of gallium-oxide-based solar-blind ultraviolet photodetectors. *Photonics Res.* **2019**, *7*, 381–415. [[CrossRef](#)]
5. Hou, X.H.; Zou, Y.N.; Ding, M.F.; Qin, Y.; Zhang, Z.F.; Ma, X.L.; Tan, P.J.; Yu, S.J.; Zhou, X.Z.; Zhao, X.L.; et al. Review of polymorphous Ga₂O₃ materials and their solar-blind photodetector applications. *J. Phys. D Appl. Phys.* **2021**, *54*, 043001. [[CrossRef](#)]
6. Liang, H.L.; Han, Z.Y.; Mei, Z.X. Recent Progress of Deep Ultraviolet Photodetectors using Amorphous Gallium Oxide Thin Films. *Phys. Status Solidi A* **2021**, *218*, 2000339. [[CrossRef](#)]
7. Monroy, E.; Omnès, F.; Calle, F. Wide-bandgap semiconductor ultraviolet photodetectors. *Semicond. Sci. Technol.* **2003**, *18*, R33–R51. [[CrossRef](#)]
8. Qin, Y.; Li, L.; Zhao, X.; Tompa, G.S.; Dong, H.; Jian, G.; He, Q.M.; Tan, P.; Hou, X.; Zhang, Z.; et al. Metal-Semiconductor-Metal ϵ -Ga₂O₃ Solar-Blind Photodetectors with a Record-High Responsivity Rejection Ratio and Their Gain Mechanism. *ACS Photonics* **2020**, *7*, 812–820. [[CrossRef](#)]
9. Zhang, H.C.; Liang, F.Z.; Song, K.; Xing, C.; Wang, D.H.; Yu, H.B.; Huang, C.; Sun, Y.; Yang, L.; Zhao, X.L.; et al. Demonstration of AlGa_N/Ga_N-based ultraviolet phototransistor with a record high responsivity over 3.6×10^7 A/W. *Appl. Phys. Lett.* **2021**, *118*, 242105. [[CrossRef](#)]
10. Fan, M.M.; Liu, K.W.; Chen, X.; Wang, X.; Zhang, Z.Z.; Li, B.H.; Shen, D.Z. Mechanism of Excellent Photoelectric Characteristics in Mixed-Phase ZnMgO Ultraviolet Photodetectors with Single Cutoff Wavelength. *ACS Appl. Mater. Interfaces* **2015**, *7*, 20600–20606. [[CrossRef](#)]
11. Chen, Y.; Lu, Y.; Lin, C.; Tian, Y.; Gao, C.; Dong, L.; Shan, C. Self-powered diamond/ β -Ga₂O₃ photodetectors for solar-blind imaging. *J. Mater. Chem. C* **2018**, *6*, 5727–5732. [[CrossRef](#)]
12. Chikoidze, E.; Tchelidze, T.; Sartel, C.; Chi, Z.; Kabouche, R.; Madaci, I.; Rubio, C.; Mohamed, H.; Sallet, V.; Medjdoub, F.; et al. Ultra-high critical electric field of 13.2 MV/cm for Zn-doped p-type β -Ga₂O₃. *Mater. Today Phys.* **2020**, *15*, 100263. [[CrossRef](#)]
13. Feng, W.; Wang, X.N.; Zhang, J.; Wang, L.F.; Zheng, W.; Hu, P.A.; Cao, W.W.; Yang, B. Synthesis of two-dimensional β -Ga₂O₃ nanosheets for high-performance solar blind photodetectors. *J. Mater. Chem. C* **2014**, *2*, 3254–3259. [[CrossRef](#)]
14. Zhang, D.; Zheng, W.; Lin, R.C.; Li, T.T.; Zhang, Z.J.; Huang, F. High quality β -Ga₂O₃ film grown with N₂O for high sensitivity solar-blind-ultraviolet photodetector with fast response speed. *J. Alloys Compd.* **2018**, *735*, 150–154. [[CrossRef](#)]
15. Zhang, M.M.; Kang, S.; Zhang, K.; Wu, Y.T.; Feng, S.L.; Lu, W.Q. Facile Synthesis of β -Ga₂O₃ nanowires network for solar-blind ultraviolet photodetector. *J. Phys. D: Appl. Phys.* **2021**, *54*, 175106. [[CrossRef](#)]

16. Hou, X.H.; Sun, H.D.; Long, S.B.; Tompa, G.S.; Salagaj, T.; Qin, Y.; Zhang, Z.F.; Tan, P.J.; Yu, S.J.; Liu, M. Ultrahigh-Performance Solar-Blind Photodetector Based on α -Phase-Dominated Ga_2O_3 Film With Record Low Dark Current of 81 fA. *IEEE Electron. Device Lett.* **2019**, *40*, 1483–1486. [[CrossRef](#)]
17. Wu, C.; He, C.; Guo, D.; Zhang, F.; Li, P.; Wang, S.; Liu, A.; Wu, F.; Tang, W. Vertical α/β - Ga_2O_3 phase junction nanorods array with graphene-silver nanowire hybrid conductive electrode for high-performance self-powered solar-blind photodetectors. *Mater. Today Phys.* **2020**, *12*, 100193. [[CrossRef](#)]
18. Cui, S.; Mei, Z.; Zhang, Y.; Liang, H.; Du, X. Room-Temperature Fabricated Amorphous Ga_2O_3 High-Response-Speed Solar-Blind Photodetector on Rigid and Flexible Substrates. *Adv. Opt. Mater.* **2017**, *5*, 1700454. [[CrossRef](#)]
19. Teng, Y.; Song, X.; Ponchel, A.; Yang, Z.K.; Xia, J. Self-assembled metastable γ - Ga_2O_3 nanoflowers with hexagonal nanopetals for solar-blind photodetection. *Adv. Mater.* **2014**, *26*, 6238–6243. [[CrossRef](#)]
20. Kong, W.Y.; Wu, G.A.; Wang, K.Y.; Zhang, T.F.; Zou, Y.F.; Wang, D.D.; Luo, L.B. Graphene- β - Ga_2O_3 Heterojunction for Highly Sensitive Deep UV Photodetector Application. *Adv. Mater.* **2016**, *28*, 10725–10731. [[CrossRef](#)] [[PubMed](#)]
21. Oshima, T.; Okuno, T.; Arai, N.; Suzuki, N.; Ohira, S.; Fujita, S. Vertical Solar-Blind Deep-Ultraviolet Schottky Photodetectors Based on β - Ga_2O_3 Substrates. *Appl. Phys. Express* **2008**, *1*, 011202. [[CrossRef](#)]
22. Li, Y.; Tokizono, T.; Liao, M.; Zhong, M.; Koide, Y.; Yamada, I.; Delaunay, J.J. Efficient Assembly of Bridged β - Ga_2O_3 Nanowires for Solar-Blind Photodetection. *Adv. Funct. Mater.* **2010**, *20*, 3972–3978. [[CrossRef](#)]
23. Wang, D.H.; Liu, X.; Fang, S.; Huang, C.; Kang, Y.; Yu, H.B.; Liu, Z.L.; Zhang, H.C.; Long, R.; Xiong, Y.J.; et al. Pt/AlGaIn Nanoarchitecture: Toward High Responsivity, Self-Powered Ultraviolet-Sensitive Photodetection. *Nano Lett.* **2020**, *21*, 120–129. [[CrossRef](#)] [[PubMed](#)]
24. Gong, H.H.; Yu, X.X.; Xu, Y.; Chen, X.H.; Kuang, Y.; Lv, Y.J.; Yang, Y.; Ren, F.F.; Feng, Z.H.; Gu, S.L.; et al. β - Ga_2O_3 vertical heterojunction barrier Schottky diodes terminated with p-NiO field limiting rings. *Appl. Phys. Lett.* **2021**, *118*, 202102. [[CrossRef](#)]
25. Qian, L.; Wu, Z.; Zhang, Y.; Lai, P.; Liu, X.; Li, Y. Ultrahigh-Responsivity, Rapid-Recovery, Solar-Blind Photodetector Based on Highly Nonstoichiometric Amorphous Gallium Oxide. *ACS Photonics* **2017**, *4*, 2203–2211. [[CrossRef](#)]
26. Wong, M.H.; Murakami, H.; Kumagai, Y.; Higashiwaki, M. Aperture-limited conduction and its possible mechanism in ion-implanted current aperture vertical β - Ga_2O_3 MOSFETs. *Appl. Phys. Lett.* **2021**, *118*, 012102. [[CrossRef](#)]
27. Mukhopadhyay, P.; Schoenfeld, W.V. Tin Gallium Oxide Solar-Blind Photodetectors on Sapphire Grown by Molecular Beam Epitaxy. *Appl. Opt.* **2019**, *58*, D22–D27. [[CrossRef](#)] [[PubMed](#)]
28. Han, S.; Hu, S.R.; Cao, P.J.; Liu, W.J.; Zeng, Y.X.; Jia, F.; Xu, W.Y.; Liu, X.K.; Zhu, D.L.; Lu, Y.M. High signal/noise ratio deep UV detector with maximum response at 230 nm based on mix-phase MgZnO deposited under high laser energy condition. *Europhys. Lett.* **2018**, *124*, 18006. [[CrossRef](#)]
29. Fan, M.M.; Liu, K.W.; Zhang, Z.Z.; Li, B.H.; Chen, X.; Zhao, D.X.; Shan, C.X.; Shen, D.Z. High-performance solar-blind ultraviolet photodetector based on mixed-phase ZnMgO thin film. *Appl. Phys. Lett.* **2014**, *105*, 011117. [[CrossRef](#)]
30. Lee, S.H.; Kim, S.B.; Moon, Y.-J.; Kim, S.M.; Jung, H.J.; Seo, M.S.; Lee, K.M.; Kim, S.-K.; Lee, S.W. High-Responsivity Deep-Ultraviolet-Selective Photodetectors Using Ultrathin Gallium Oxide Films. *ACS Photonics* **2017**, *4*, 2937–2943. [[CrossRef](#)]
31. Sun, H.L.; Zhang, L.Y.; Yu, J.Y.; Wang, S.L.; Guo, D.Y.; Li, C.R.; Wu, F.M.; Liu, A.P.; Li, P.G.; Tang, W.H. Phase junction enhanced photocatalytic activity of Ga_2O_3 nanorod arrays on flexible glass fiber fabric. *RSC Adv.* **2020**, *10*, 11499–11506. [[CrossRef](#)]
32. Wang, X.; Xu, Q.; Li, M.; Shen, S.; Wang, X.; Wang, Y.; Feng, Z.; Shi, J.; Han, H.; Li, C. Photocatalytic Overall Water Splitting Promoted by an α - β phase Junction on Ga_2O_3 . *Angew. Chem. Int. Ed.* **2012**, *51*, 13089–13092. [[CrossRef](#)]
33. Lu, Y.M.; Li, C.; Chen, X.H.; Han, S.; Cao, P.J.; Jia, F.; Zeng, Y.X.; Liu, X.K.; Xu, W.Y.; Liu, W.J.; et al. Preparation of Ga_2O_3 thin film solar-blind photodetectors based on mixed-phase structure by pulsed laser deposition. *Chin. Phys. B* **2019**, *28*, 018504. [[CrossRef](#)]
34. Kumar, S.S.; Rubio, E.J.; Noor-A-Alam, M.; Martinez, G.; Manandhar, S.; Shutthanandan, V.; Thevuthasan, S.; Ramana, C.V. Structure, Morphology, and Optical Properties of Amorphous and Nanocrystalline Gallium Oxide Thin Films. *J. Phys. Chem. C* **2013**, *117*, 4194–4200. [[CrossRef](#)]
35. Wang, Y.H.; Cui, W.J.; Yu, J.; Zhi, Y.S.; Li, H.R.; Hu, Z.Y.; Sang, X.H.; Guo, E.J.; Tang, W.H.; Wu, Z.P. One-Step Growth of Amorphous/Crystalline Ga_2O_3 Phase-Junctions for High-Performance Solar-Blind Photodetection. *ACS Appl. Mater. Interfaces* **2019**, *11*, 45922–45929. [[CrossRef](#)]
36. Kranert, C.; Sturm, C.; Schmidt-Grund, R.; Grundmann, M. Raman tensor elements of β - Ga_2O_3 . *Sci. Rep.* **2016**, *6*, 35964. [[CrossRef](#)]
37. Du, J.L.; Fang, Y.; Fu, E.G.; Ding, X.; Yu, K.Y.; Wang, Y.G.; Wang, Y.Q.; Baldwin, J.K.; Wang, P.P.; Bai, Q. What determines the interfacial configuration of Nb/ Al_2O_3 and Nb/ MgO interface. *Sci. Rep.* **2016**, *6*, 33931. [[CrossRef](#)] [[PubMed](#)]
38. Mohamed, M.; Irmscher, K.; Janowitz, C.; Galazka, Z.; Manzke, R.; Fornari, R. Schottky barrier height of Au on the transparent semiconducting oxide β - Ga_2O_3 . *Appl. Phys. Lett.* **2012**, *101*, 132106. [[CrossRef](#)]
39. Xu, X.; Chen, J.; Cai, S.; Long, Z.; Zhang, Y.; Su, L.; He, S.; Tang, C.; Liu, P.; Peng, H.; et al. A Real-Time Wearable UV-Radiation Monitor based on a High-Performance p-CuZnS/n-TiO₂ Photodetector. *Adv. Mater.* **2018**, *30*, 1803165. [[CrossRef](#)] [[PubMed](#)]
40. Oh, S.; Kim, C.-K.; Kim, J. High Responsivity β - Ga_2O_3 Metal-Semiconductor-Metal Solar-Blind Photodetectors with Ultraviolet Transparent Graphene Electrodes. *ACS Photonics* **2017**, *5*, 1123–1128. [[CrossRef](#)]
41. Guo, P.; Xiong, J.; Zhao, X.H.; Sheng, T.; Yue, C.; Tao, B.W.; Liu, X.Z. Growth characteristics and device properties of MOD derived β - Ga_2O_3 films. *J. Mater. Sci. Mater. Electron.* **2014**, *25*, 3629–3632. [[CrossRef](#)]

42. Zhuo, R.R.; Wu, D.; Wang, Y.G.; Wu, E.P.; Jia, C.; Shi, Z.F.; Xu, T.T.; Tian, Y.T.; Li, X.J. A self-powered solar-blind photodetector based on a MoS₂/β-Ga₂O₃ heterojunction. *J. Mater. Chem. C* **2018**, *6*, 10982–10986. [[CrossRef](#)]
43. Zhao, B.; Wang, F.; Chen, H.; Zheng, L.; Su, L.; Zhao, D.; Fang, X. An Ultrahigh Responsivity (9.7 mA W⁻¹) Self-Powered Solar-Blind Photodetector Based on Individual ZnO-Ga₂O₃ Heterostructures. *Adv. Funct. Mater.* **2017**, *27*, 1700264. [[CrossRef](#)]
44. Wu, Z.P.; Jiao, L.; Wang, X.L.; Guo, D.Y.; Li, W.H.; Li, L.H.; Huang, F.; Tang, W.H. A self-powered deep-ultraviolet photodetector based on an epitaxial Ga₂O₃/Ga: ZnO heterojunction. *J. Mater. Chem. C* **2017**, *5*, 8688–8693. [[CrossRef](#)]
45. Cai, J.; Xu, X.J.; Su, L.X.; Yang, W.; Chen, H.Y.; Zhang, Y.; Fang, X.S. Self-Powered n-SnO₂/p-CuZnS Core-Shell Microwire UV Photodetector with Optimized Performance. *Adv. Opt. Mater.* **2018**, *6*, 1800213. [[CrossRef](#)]
46. Guo, D.; Su, Y.; Shi, H.; Li, P.; Zhao, N.; Ye, J.; Wang, S.; Liu, A.; Chen, Z.; Li, C.; et al. Self-Powered Ultraviolet Photodetector with Superhigh Photoresponsivity (3.05 A/W) Based on the GaN/Sn: Ga₂O₃ pn Junction. *ACS Nano* **2018**, *12*, 12827–12835. [[CrossRef](#)]
47. Li, S.; Guo, D.; Li, P.G.; Wang, X.; Wang, Y.; Yan, Z.; Liu, Z.; Zhi, Y.; Huang, Y.; Wu, Z.; et al. Ultrasensitive, Superhigh Signal-to-Noise Ratio, Self-Powered Solar-Blind Photodetector Based on n-Ga₂O₃/p-CuSCN Core-Shell Microwire Heterojunction. *ACS Appl. Mater. Interfaces* **2019**, *11*, 35105–35114. [[CrossRef](#)] [[PubMed](#)]
48. Zheng, W.; Lin, R.C.; Ran, J.X.; Zhang, Z.J.; Ji, X.; Huang, F. Vacuum-Ultraviolet Photovoltaic Detector. *ACS Nano* **2018**, *12*, 425–431. [[CrossRef](#)] [[PubMed](#)]
49. Xu, X.; Hu, J.; Yin, Z.; Xu, C. Photoanode current of large-area MoS₂ ultrathin nanosheets with vertically mesh-shaped structure on indium tin oxide. *ACS Appl. Mater. Interfaces* **2014**, *6*, 5983–5987. [[CrossRef](#)] [[PubMed](#)]
50. Arora, K.; Goel, N.; Kumar, M.; Kumar, M. Ultrahigh Performance of Self-Powered β-Ga₂O₃ Thin Film Solar-Blind Photodetector Grown on Cost-Effective Si Substrate Using High-Temperature Seed Layer. *ACS Photonics* **2018**, *5*, 2391–2401. [[CrossRef](#)]
51. Wheeler, V.D.; Shahin, D.I.; Tadjer, M.J.; Eddy, C.R., Jr. Band alignments of atomic layer deposited ZrO₂ and HfO₂ high-k dielectrics with (-201) β-Ga₂O₃. *ECS J. Solid State Sci. Technol.* **2016**, *6*, Q3052–Q3055. [[CrossRef](#)]
52. Carey, P.H., IV; Ren, F.; Hays, D.C.; Gila, B.; Pearton, S.; Jang, S.; Kuramata, A. Band offsets in ITO/Ga₂O₃ heterostructures. *Appl. Surf. Sci.* **2017**, *422*, 179–183. [[CrossRef](#)]
53. Kraut, E.A.; Grant, R.W.; Waldrop, J.R.; Kowalczyk, S.P. Precise Determination of the Valence-Band Edge in X-Ray Photoemission Spectra: Application to Measurement of Semiconductor Interface Potentials. *Phys. Rev. Lett.* **1980**, *44*, 1620–1623. [[CrossRef](#)]
54. Seul, H.J.; Kim, M.J.; Yang, H.J.; Cho, M.H.; Cho, M.H.; Song, W.B.; Jeong, J.K. Atomic Layer Deposition Process-Enabled Carrier Mobility Boosting in Field-Effect Transistors through a Nanoscale ZnO/IGO Heterojunction. *ACS Appl. Mater. Interfaces* **2020**, *12*, 33887–33898. [[CrossRef](#)]
55. Gao, W.; Zheng, Z.; Huang, L.; Yao, J.; Zhao, Y.; Xiao, Y.; Li, J. Self-Powered SnS_{1-x}Se_x Alloy/Silicon Heterojunction Photodetectors with High Sensitivity in a Wide Spectral Range. *ACS Appl. Mater. Interfaces* **2019**, *11*, 40222–40231. [[CrossRef](#)]
56. Kalra, A.; Vura, S.; Rathkanthiwar, S.; Muralidharan, R.; Raghavan, S.; Nath, D.N. Demonstration of high-responsivity epitaxial β-Ga₂O₃/GaN metal-heterojunction-metal broadband UV-A/UV-C detector. *Appl. Phys. Express* **2018**, *11*, 064101. [[CrossRef](#)]
57. Chen, J.X.; Tao, J.J.; Ma, H.P.; Zhang, H.; Feng, J.J.; Liu, W.J.; Xia, C.T.; Lu, H.L.; Zhang, D.W. Band alignment of AlN/β-Ga₂O₃ heterojunction interface measured by x-ray photoelectron spectroscopy. *Appl. Phys. Lett.* **2018**, *112*, 261602. [[CrossRef](#)]
58. Castanedo, C.G.T.; Li, K.H.; Braic, L.; Li, X.H. Determination of band offsets of Ga₂O₃/FTO heterojunction for current spreading applications. *J. Phys. D Appl. Phys.* **2020**, *53*, 314003. [[CrossRef](#)]
59. Xu, Y.; You, Y.; Huang, H.W.; Guo, Y.X.; Zhang, Y.H. Bi₄NbO₈Cl {001} nanosheets coupled with g-C₃N₄ as 2D/2D heterojunction for photocatalytic degradation and CO₂ reduction. *J. Hazard. Mater.* **2020**, *381*, 121159. [[CrossRef](#)] [[PubMed](#)]
60. Carey, P.H.; Ren, F.; Hays, D.C.; Gila, B.P.; Pearton, S.J.; Jang, S.; Kuramata, A. Valence and conduction band offsets in AZO/Ga₂O₃ heterostructures. *Vacuum* **2017**, *141*, 103–108. [[CrossRef](#)]
61. Sun, S.M.; Liu, W.J.; Wang, Y.P.; Huan, Y.W.; Ma, Q.; Zhu, B.; Wu, S.D.; Yu, W.J.; Horng, R.H.; Xia, C.T. Band alignment of In₂O₃/β-Ga₂O₃ interface determined by X-ray photoelectron spectroscopy. *Appl. Phys. Lett.* **2018**, *113*, 031603. [[CrossRef](#)]
62. Huan, Y.W.; Wang, X.L.; Liu, W.J.; Dong, H.; Long, S.B.; Sun, S.M.; Yang, J.G.; Wu, S.D.; Yu, W.J.; Horng, R.H. Band alignment of indium-gallium-zinc oxide/β-Ga₂O₃ heterojunction determined by angle-resolved X-ray photoelectron spectroscopy. *Jpn. J. Appl. Phys.* **2018**, *57*, 100312. [[CrossRef](#)]
63. Maccioni, M.B.; Ricci, F.; Fiorentini, V. Low In solubility and band offsets in the small-x β-Ga₂O₃/(Ga_{1-x}In_x)₂O₃ system. *Appl. Phys. Express* **2015**, *8*, 021102. [[CrossRef](#)]
64. Yang, S.J.; Liu, K.L.; Han, W.; Li, L.; Wang, F.K.; Zhou, X.; Li, H.Q.; Zhai, T.Y. Salt-Assisted Growth of P-type Cu₉S₅ Nanoflakes for P-N Heterojunction Photodetectors with High Responsivity. *Adv. Funct. Mater.* **2019**, *30*, 1908382. [[CrossRef](#)]
65. Wei, Y.D.; Wang, T.Q.; Zhang, Y.Q.; Qi, C.H.; Luan, J.; Ma, G.L.; Tsai, H.-S.; Liu, C.M.; Huo, M.X. Effects of carbon related defects on opto-electronic properties of β-Ga₂O₃: The first principle calculation. *Results Phys.* **2020**, *17*, 103060. [[CrossRef](#)]
66. Mulazzi, M.; Reichmann, F.; Becker, A.; Klesse, W.M.; Alippi, P.; Fiorentini, V.; Parisini, A.; Bosi, M.; Fornari, R. The electronic structure of ε-Ga₂O₃. *APL Mater.* **2019**, *7*, 022522. [[CrossRef](#)]
67. Sun, S.M.; Liu, W.J.; Golosov, D.A.; Gu, C.J.; Ding, S.J. Investigation of energy band at atomic layer deposited AZO/β-Ga₂O₃ (-201) heterojunctions. *Nanoscale Res. Lett.* **2019**, *14*, 412. [[CrossRef](#)]
68. Zhang, Z.D.; Ding, Z.; Guo, X.; Luo, Z.J.; Wei, J.M.; Yang, C.; Huang, Y.B.; Li, Z.H. First-principle calculations of electronic and optical properties of Ti-doped β-Ga₂O₃ with intrinsic defects. *Mater. Res. Express* **2019**, *6*, 105920. [[CrossRef](#)]
69. Schubert, M.; Mock, A.; Korlacki, R.; Knight, S.; Galazka, Z.; Wagner, G.; Wheeler, V.; Tadjer, M.; Goto, K.; Darakchieva, V. Longitudinal phonon plasmon mode coupling in β-Ga₂O₃. *Appl. Phys. Lett.* **2019**, *114*, 102102. [[CrossRef](#)]

-
70. Jiang, Z.X.; Wu, Z.Y.; Ma, C.C.; Deng, J.N.; Zhang, H.; Xu, Y.; Ye, J.D.; Fang, Z.L.; Zhang, G.Q.; Kang, J.Y.; et al. P-type β -Ga₂O₃ metal-semiconductor-metal solar-blind photodetectors with extremely high responsivity and gain-bandwidth product. *Mater. Today Phys.* **2020**, *14*, 100226. [[CrossRef](#)]
 71. Katz, O.; Garber, V.; Meyler, B.; Bahir, G.; Salzman, J. Gain mechanism in GaN Schottky ultraviolet detectors. *Appl. Phys. Lett.* **2001**, *79*, 1417–1419. [[CrossRef](#)]
 72. Clavero, C. Plasmon-induced hot-electron generation at nanoparticle/metal-oxide interfaces for photovoltaic and photocatalytic devices. *Nat. Photonics* **2014**, *8*, 95–103. [[CrossRef](#)]